

# Sunlight-driven nitrate loss records Antarctic surface mass balance

**Pete D. Akers** (✉ [pete.d.akers@gmail.com](mailto:pete.d.akers@gmail.com))

Université Grenoble Alpes, CNRS, IRD, Grenoble INP, IGE, Grenoble, France <https://orcid.org/0000-0002-2266-5551>

**Joël Savarino**

Université Grenoble Alpes, CNRS, IRD, Grenoble INP, IGE, Grenoble, France

**Nicolas Caillon**

Université Grenoble Alpes, CNRS, IRD, Grenoble INP, IGE, Grenoble, France

**Aymeric P. M. Servettaz**

Japan Agency for Marine-Earth Science and Technology, Yokosuka, Japan

**Emmanuel Le Meur**

Université Grenoble Alpes, CNRS, IRD, Grenoble INP, IGE, Grenoble, France

**Olivier Magand**

Université Grenoble Alpes, CNRS, IRD, Grenoble INP, IGE, Grenoble, France

**Jean Martins**

Université Grenoble Alpes, CNRS, IRD, Grenoble INP, IGE, Grenoble, France

**Cécile Agosta**

Laboratoire des Sciences du Climat et de l'Environnement, LSCE-IPSL, CEA-CNRS-UVSQ, Université Paris-Saclay, Gif-sur-Yvette, France <https://orcid.org/0000-0003-4091-1653>

**Peter Crockford**

Department of Earth and Planetary Sciences, Weizmann Institute of Science, Rehovot, Israel;  
Department of Earth and Planetary Sciences, Harvard University, Cambridge, MA, USA

**Kanon Kobayashi**

Department of Chemical Science and Engineering, Tokyo Institute of Technology, Yokohama, Japan

**Shohei Hattori**

Department of Chemical Science and Engineering, Tokyo Institute of Technology, Yokohama, Japan;  
International Center for Isotope Effects Research, Nanjing University, Nanjing, China

**Mark Curran**

Australian Antarctic Division, Department of Agriculture, Water and Environment, Kingston, Tasmania, Australia; Australian Antarctic Program Partnership, Institute of Marine and Antarctic Studies, University of Tasmania, Hobart, Tasmania, Australia

**Tas van Ommen**

Australian Antarctic Division, Department of Agriculture, Water and Environment, Kingston, Tasmania, Australia; Australian Antarctic Program Partnership, Institute of Marine and Antarctic Studies, University

of Tasmania, Hobart, Tasmania, Australia <https://orcid.org/0000-0002-2463-1718>

### **Lenneke Jong**

Australian Antarctic Division, Department of Agriculture, Water and Environment, Kingston, Tasmania, Australia; Australian Antarctic Program Partnership, Institute of Marine and Antarctic Studies, University of Tasmania, Hobart, Tasmania, Australia

### **Jason L. Roberts**

Australian Antarctic Division, Department of Agriculture, Water and Environment, Kingston, Tasmania, Australia; Australian Antarctic Program Partnership, Institute of Marine and Antarctic Studies, University of Tasmania, Hobart, Tasmania, Australia

---

## **Article**

### **Keywords:**

**Posted Date:** February 8th, 2022

**DOI:** <https://doi.org/10.21203/rs.3.rs-1307003/v1>

**License:**  This work is licensed under a Creative Commons Attribution 4.0 International License.

[Read Full License](#)

---

**Version of Record:** A version of this preprint was published at Nature Communications on July 25th, 2022. See the published version at <https://doi.org/10.1038/s41467-022-31855-7>.

## Sunlight-driven nitrate loss records Antarctic surface mass balance

**Authors:** Pete D. Akers<sup>1\*</sup>, Joël Savarino<sup>1\*</sup>, Nicolas Caillon<sup>1</sup>, Aymeric P. M. Servettaz<sup>2</sup>, Emmanuel Le Meur<sup>1</sup>, Olivier Magand<sup>1</sup>, Jean Martins<sup>1</sup>, Cécile Agosta<sup>3</sup>, Peter Crockford<sup>4,5</sup>, Kanon Kobayashi<sup>6</sup>, Shohei Hattori<sup>6,7</sup>, Mark Curran<sup>8,9</sup>, Tas van Ommen<sup>8,9</sup>, Lenneke Jong<sup>8,9</sup>, Jason L. Roberts<sup>8,9</sup>

### Affiliations:

<sup>1</sup>Université Grenoble Alpes, CNRS, IRD, Grenoble INP, IGE, Grenoble, France.

<sup>2</sup>Japan Agency for Marine-Earth Science and Technology, Yokosuka, Japan.

<sup>3</sup>Laboratoire des Sciences du Climat et de l'Environnement, LSCE-IPSL, CEA-CNRS-UVSQ, Université Paris-Saclay, Gif-sur-Yvette, France.

<sup>4</sup>Department of Earth and Planetary Sciences, Weizmann Institute of Science, Rehovot, Israel.

<sup>5</sup>Department of Earth and Planetary Sciences, Harvard University, Cambridge, MA, USA.

<sup>6</sup>Department of Chemical Science and Engineering, Tokyo Institute of Technology, Yokohama, Japan.

<sup>7</sup>International Center for Isotope Effects Research, Nanjing University, Nanjing, China.

<sup>8</sup>Australian Antarctic Division, Department of Agriculture, Water and Environment, Kingston, Tasmania, Australia.

<sup>9</sup>Australian Antarctic Program Partnership, Institute of Marine and Antarctic Studies, University of Tasmania, Hobart, Tasmania, Australia.

\*Correspondence to: [pete-akers@univ-grenoble-alpes.fr](mailto:pete-akers@univ-grenoble-alpes.fr); [joel.savarino@cnrs.fr](mailto:joel.savarino@cnrs.fr)

### Abstract:

Standard proxies for reconstructing surface mass balance (SMB) in Antarctic ice cores are often inaccurate or coarsely resolved when applied to more complicated environments away from dome summits. Here, we propose an alternative SMB proxy based on photolytic fractionation of nitrogen isotopes in nitrate observed at 114 sites throughout East Antarctica. Applying this proxy approach to nitrate in a shallow core drilled at a moderate SMB site (Aurora Basin North), we reconstruct 700 years of SMB changes that agree well with changes estimated from ice core density and upstream surface topography. For the under-sampled transition zones between dome summits and the coast, this proxy can considerably

expand our SMB records by providing high-resolution SMBs that better reflect the local environment and are easier to sample than existing techniques.

35 **One Sentence Summary:** Nitrate isotopes offer a new way to track past and present changes in Antarctic snowfall and ice sheet mass balance.

**Main Text:** Antarctica holds a critical role in the Earth's hydrosphere, providing long-term storage of 27 million km<sup>3</sup> of ice<sup>1</sup> and impacting global ocean and atmosphere circulation through its albedo, topography, export of calved glacial ice, and function as an atmospheric heat sink<sup>2-5</sup>. Since even small shifts in the surface mass balance (SMB) across Antarctic ice sheets can redistribute huge masses of water between the cryosphere, ocean, and atmosphere, a clear understanding of how its SMB has responded to past climate change is crucial for calibrating forecast models of the global environment and properly interpreting ice cores<sup>6-10</sup>. Despite this pressing importance, a comprehensive understanding of past SMB changes in Antarctica is limited by insufficient long-term records for sites between of the wet coastal periphery and dry dome summits.

Reconstructing SMBs in this moderate SMB transition zone can be challenging with existing SMB proxies. Ice density-based reconstructions become less effective and more uncertain with depth due to thinning and deformation of ice layers<sup>11</sup>, while the frequent minor damage and breakage of cores during the drilling process can make accurate physical measurements of mass and volume challenging. Water isotopes ( $\delta^2\text{H}$  or  $\delta^{18}\text{O}$ ) can be used as a proxy temperature to derive snow accumulation through water vapor saturation<sup>10</sup>, but this approach does not account for wind-driven transport and sublimation of surface snow at warmer and lower elevation sites<sup>12-14</sup>. Additionally, water isotopes reflect many environmental factors other than temperature, such as atmospheric circulation changes, which can lead to large uncertainty and/or bias in reconstructed SMBs<sup>15,16</sup>. There is thus a strong need for alternative

proxies that better record local conditions to provide SMB estimates for paleoclimate reconstructions and ice sheet models.

Here, we present one such independent SMB proxy based on photolysis-induced changes in

60 the  $^{15}\text{N}/^{14}\text{N}$  ratio ( $\delta^{15}\text{N}$ , defined as  $\delta = \frac{^{15}\text{N}/^{14}\text{N}_{\text{sample}}}{^{15}\text{N}/^{14}\text{N}_{\text{standard}}} - 1$ , relative to the  $\text{N}_2$ -air standard) of

nitrate ( $\text{NO}_3^-$ ) (Figure 1). Naturally deposited on the Antarctic ice sheet surface as the end

product of the atmospheric oxidation of reactive nitrogen<sup>17–20</sup>,  $\text{NO}_3^-$  within the Antarctic

snowpack can be photolytically converted to gaseous nitrogen oxides ( $\text{NO}_x = \text{NO} + \text{NO}_2$ )

when exposed to ultraviolet light ( $\lambda = 290\text{--}350$  nm). Because  $^{14}\text{NO}_3^-$  is more readily

65 photolyzed than  $^{15}\text{NO}_3^-$ , the  $\delta^{15}\text{N}_{\text{NO}_3}$  of  $\text{NO}_3^-$  remaining in the snow will increase from its

initial depositional value of  $\approx -20$  to  $+20$  ‰ to values as high as  $+400$  ‰<sup>19–26</sup> as the

isotopically lighter photolytic  $\text{NO}_x$  is ventilated and lost to the atmosphere. Although  $\text{NO}_3^-$

can also be lost through  $\text{HNO}_3$  volatilization, we interpret  $\delta^{15}\text{N}_{\text{NO}_3\text{arc}}$  solely through

photolysis as volatilization does not strongly fractionate  $\text{NO}_3^-$  and is a very minor component

70 of  $\text{NO}_3^-$  loss outside of the warmest coastal zones<sup>22,27,28</sup>. Additionally, while the oxygen in

$\text{NO}_3^-$  also undergoes isotopic fractionation through photolysis, its interpretation is

complicated by isotopic interactions with snow and water vapor<sup>22,23,29</sup> and is not further

discussed here.

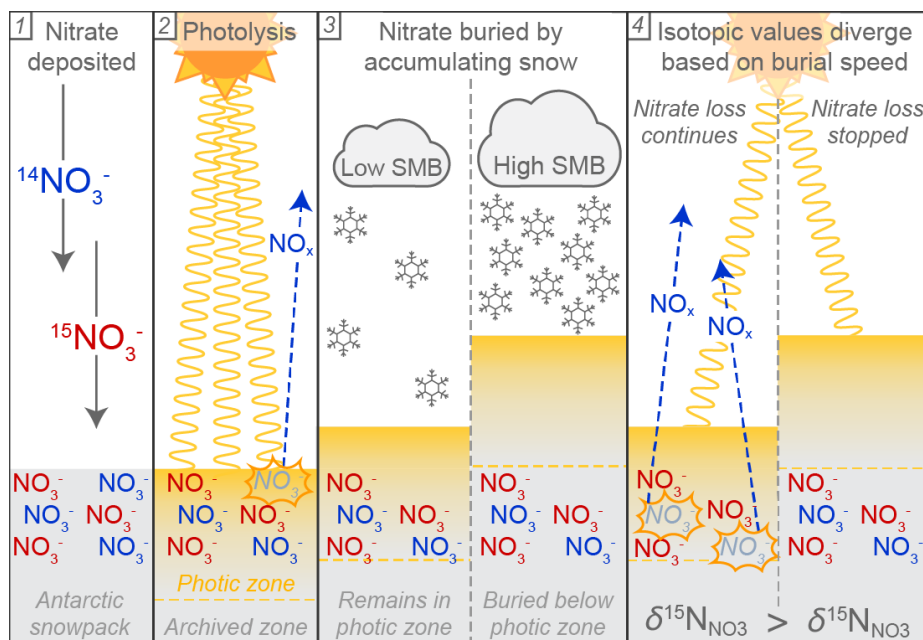


Figure 1. Schematic diagram illustrating that SMB and  $\delta^{15}\text{N}_{\text{NO}_3\text{arc}}$  values covary due to photolytic  $\text{NO}_3^-$  mass loss. After  $\text{NO}_3^-$  containing either  $^{14}\text{N}$  (blue) and  $^{15}\text{N}$  (red) is deposited on the Antarctic snowpack surface (1), sunlight in the photic zone can trigger photolysis of  $\text{NO}_3^-$  that favors  $\text{NO}_3^-$  with a  $^{14}\text{N}$  atom, which leaves the residual  $\text{NO}_3^-$  enriched in  $^{15}\text{N}$  (2). Because sites with lower SMBs will accumulate less snow over a given period of time than high SMB sites (3), the  $\text{NO}_3^-$  at lower SMB sites will remain in the photic zone longer, experience more photolytic mass loss before burial in the archived zone, and have higher  $\delta^{15}\text{N}_{\text{NO}_3\text{arc}}$  values (4).

Photolysis is limited to the depth where light penetrates and initiates photochemical reactions, and so the snowpack can be divided into an uppermost photic zone (generally 10–100 cm in East Antarctica) and a deeper archived zone<sup>29–33</sup>. Photolysis and the resulting isotopic fractionation of  $\text{NO}_3^-$  cease once snowfall buries  $\text{NO}_3^-$  beneath the photic zone, and the  $\delta^{15}\text{N}_{\text{NO}_3}$  value of the buried  $\text{NO}_3^-$  ( $\delta^{15}\text{N}_{\text{NO}_3\text{arc}}$ ) is assumed to be preserved indefinitely in glacial ice<sup>22,23,29,30</sup>. The final  $\delta^{15}\text{N}_{\text{NO}_3\text{arc}}$  value reflects the total sum of photolysis inducing radiation experienced by  $\text{NO}_3^-$  during the burial process, which, assuming stable insolation and photic zone depth, is itself determined by the rate at which the  $\text{NO}_3^-$  is buried and thus inversely related to SMB<sup>17,23,26,34</sup>. Modeling (Supplementary Text 1) and field observations support SMB as the primary driver of spatial variability in  $\delta^{15}\text{N}_{\text{NO}_3\text{arc}}$  values. Based on a new

simplified theoretical framework (Methods, Supplementary Text 1), this relationship can be expressed as:

$$\ln(\delta^{15}\text{N}_{\text{NO}_3\text{arc}} + 1) = \frac{A}{\text{SMB}} + B \quad (1)$$

95 where the regression coefficients  $A$  and  $B$  are parameters that subsume constants and linearly co-varying variables associated with photolytic and fractionation processes. The inverse function of Eq. (1) can then be used as a transfer function to reconstruct SMBs from  $\delta^{15}\text{N}_{\text{NO}_3\text{arc}}$  values ( $\text{SMB}_{\delta^{15}\text{N}}$ ).

## 100 **Results: $\text{SMB}_{\delta^{15}\text{N}}$ relationship and spatial applicability**

To obtain parameter estimates for Eq. (1), we sampled  $\text{NO}_3^-$  in snow and firn from 92 East Antarctic shallow pits and cores that are newly reported here. Combined with 43 previously published  $\delta^{15}\text{N}_{\text{NO}_3\text{arc}}$  samples<sup>21–23,26,29,35</sup>, this constitutes a database of 135 total  $\delta^{15}\text{N}_{\text{NO}_3\text{arc}}$  values representing 114 distinct sites across East Antarctica (Figure 2a). These  $\delta^{15}\text{N}_{\text{NO}_3\text{arc}}$  data were spatially paired with local SMBs either observed directly onsite ( $\text{SMB}_{\text{ground}}$ ) or as an output from the Modèle Atmosphérique Régional (MAR) using ERA-interim reanalysis data<sup>12</sup> and adjusted for a dry-site bias ( $\text{SMB}_{\text{adjMAR}}$ ) (Methods, Supplementary Text 2). The sites in our database cover a comprehensive range of East Antarctic SMBs, from 20–30 kg m<sup>-2</sup> a<sup>-1</sup> at dome summits on the high plateau to >300 kg m<sup>-2</sup> a<sup>-1</sup> for sites on the coastal periphery.

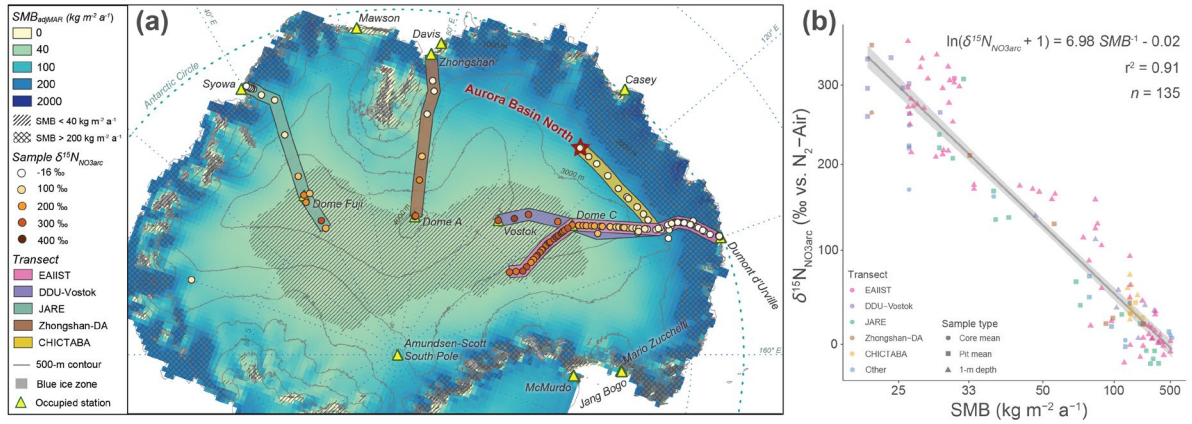


Figure 2. A) Map of East Antarctic sites sampled for  $\delta^{15}\text{N}_{\text{NO}_3\text{arc}}$  along different scientific and logistic transect routes<sup>36</sup>. The SMBs were modeled by MAR<sup>12</sup> and adjusted for dry site bias (see Methods). Regions with SMBs less than or greater than 40–200  $\text{kg m}^{-2} \text{a}^{-1}$  (i.e., the SMB range targeted by the proxy described here) are illustrated with hatching and crosshatching, respectively. Preservation of  $\text{NO}_3^-$  is not expected in blue ice zones (gray solid) due to very low or negative SMBs and wind scouring<sup>37</sup>. B) Scatter plot and linear regression of Eq. (1) using all sites in the field dataset. Note that axis labels have been converted to show simpler SMB and  $\delta^{15}\text{N}_{\text{NO}_3\text{arc}}$  values. The linear regression (gray solid line) is shown with shaded 95% confidence intervals, and regression parameters are displayed at upper right. The point colors correspond to the transect of origin shown in (a), and the point shapes correspond to the sampling method (i.e., snow core, snow pit, or 1-m depth layer).

120

The SMB and  $\delta^{15}\text{N}_{\text{NO}_3\text{arc}}$  in our field dataset are correlated with a high degree of confidence, producing a linear regression where  $\ln(\delta^{15}\text{N}_{\text{NO}_3\text{arc}} + 1) = 6.98 \pm 0.19 \text{ SMB}^{-1} - 0.02 \pm 0.01$  (Figure 2b,  $r^2 = 0.91$ ,  $p \ll 0.001$ ,  $n = 135$ ). This relationship is within modeled expectations (Figure S3, Supplementary Text 1) and reproduces the spatial variability of  $\delta^{15}\text{N}_{\text{NO}_3\text{arc}}$  observed throughout East Antarctica (Table S6). Although millennial-scale changes in global nitrogen dynamics and atmospheric oxidative capacity are not currently well known, the  $\text{SMB}_{\delta^{15}\text{N}}$  proxy should be broadly applicable to Holocene-age ice as the factors parameterized in Eq. (1) have likely been relatively stable during this time (Supplementary Text 1). For pre-Holocene ice,  $\delta^{15}\text{N}_{\text{NO}_3\text{arc}}$  can still offer important insight into relative

125

130 changes in SMB and into how nitrate dynamics varied during the dramatically different  
Antarctic and global environments of the Pleistocene.

While our field dataset covers sites with SMBs from 22 to 548 kg m<sup>-2</sup> a<sup>-1</sup>, the SMB<sub>δ15N</sub> proxy  
appears best suited for sites with SMBs between 40 and 200 kg m<sup>-2</sup> a<sup>-1</sup>. Shallow cores from  
very dry Dome A and Dome C have lower δ<sup>15</sup>N<sub>NO3arc</sub> values at 2–6 m below the surface than  
135 at the ~1 m base of the photic zone, possibly because photolytic NO<sub>x</sub> can be transported  
downward through firn air convection and re-oxidized into NO<sub>3</sub><sup>-</sup> with low δ<sup>15</sup>N<sub>NO3</sub> values  
(Supplementary Text 3, Figure S5). Although this phenomenon violates the foundational  
assumption of “locked-in” NO<sub>3</sub><sup>-</sup> beneath the photic zone, we observe only it at the ultra-dry  
interior sites where SMB > 40 kg m<sup>-2</sup> a<sup>-1</sup>. For sites with SMB > 200 kg m<sup>-2</sup> a<sup>-1</sup>, the expected  
140 δ<sup>15</sup>N<sub>NO3arc</sub> value falls within the general range of atmospheric δ<sup>15</sup>N<sub>NO3</sub> (<+20 ‰) because  
NO<sub>3</sub><sup>-</sup> is buried below the photic zone in less than a year. Since more than 80% of NO<sub>3</sub><sup>-</sup> is  
deposited during months with sunshine outside of winter polar night<sup>22,38</sup>, samples that  
integrate multiple years of accumulation at high SMB sites might still resolve differences in  
SMB, but the greater HNO<sub>3</sub> volatilization at these warmer and wetter sites also warrant  
145 caution due to possible interference. Additionally, the asymptotic nature of SMB<sup>-1</sup> means that  
δ<sup>15</sup>N<sub>NO3arc</sub> values are increasingly less sensitive to SMB changes with higher SMB values.  
Despite these restrictions, over 59 % of Antarctica has a SMB between 40 and 200 kg m<sup>-2</sup> a<sup>-1</sup>  
<sup>12</sup> (Figure 2), and additional study of NO<sub>3</sub><sup>-</sup> dynamics in wet and dry extremes may reveal  
regional adjustments that allow our proxy’s SMB range to be expanded.

150

### **Results: Aurora Basin North SMB reconstruction**

As a proof of concept, we applied the SMB<sub>δ15N</sub> transfer function to δ<sup>15</sup>N<sub>NO3arc</sub> data from the  
103 m deep ABN1314-103 ice core. This core was one of three drilled in the Australian

Antarctic Program's 2013–2014 summer campaign at Aurora Basin North (ABN; 71.17 °S  
155 111.37 °E, 2679 m above sea level), a site with moderate modern SMBs ( $\approx 120 \text{ kg m}^{-2} \text{ a}^{-1}$ )  
located midway between coastal Casey Station and the Dome C summit (Figure 2a). The  
SMB $_{\delta^{15}\text{N}}$  history reconstructed from ABN1314-103 covers the period from –47 to 649 years  
before present (BP, where present = 1950 CE) and has values ranging from 49 to 208  $\text{kg m}^{-2}$   
a $^{-1}$  (Figure 3a). Each SMB $_{\delta^{15}\text{N}}$  value integrates an average of 2.4 years of accumulation (total  
160 range: 0.7–4.5 years), and thus any impacts from individual precipitation events or seasonal  
extremes are largely moderated. Overall, the SMBs have fairly high variability (coefficient of  
variation = 0.21). The mean SMB $_{\delta^{15}\text{N}}$  in the 20<sup>th</sup> century ( $126 \pm 26.5 \text{ kg m}^{-2} \text{ a}^{-1}$ ) is 34% greater  
than the mean SMB $_{\delta^{15}\text{N}}$  before 1900 CE ( $94 \pm 18 \text{ kg m}^{-2} \text{ a}^{-1}$ ) and nearly 52% greater than the  
driest century that spans the 1600s CE ( $83 \pm 20 \text{ kg m}^{-2} \text{ a}^{-1}$ ) (Figure 3a).

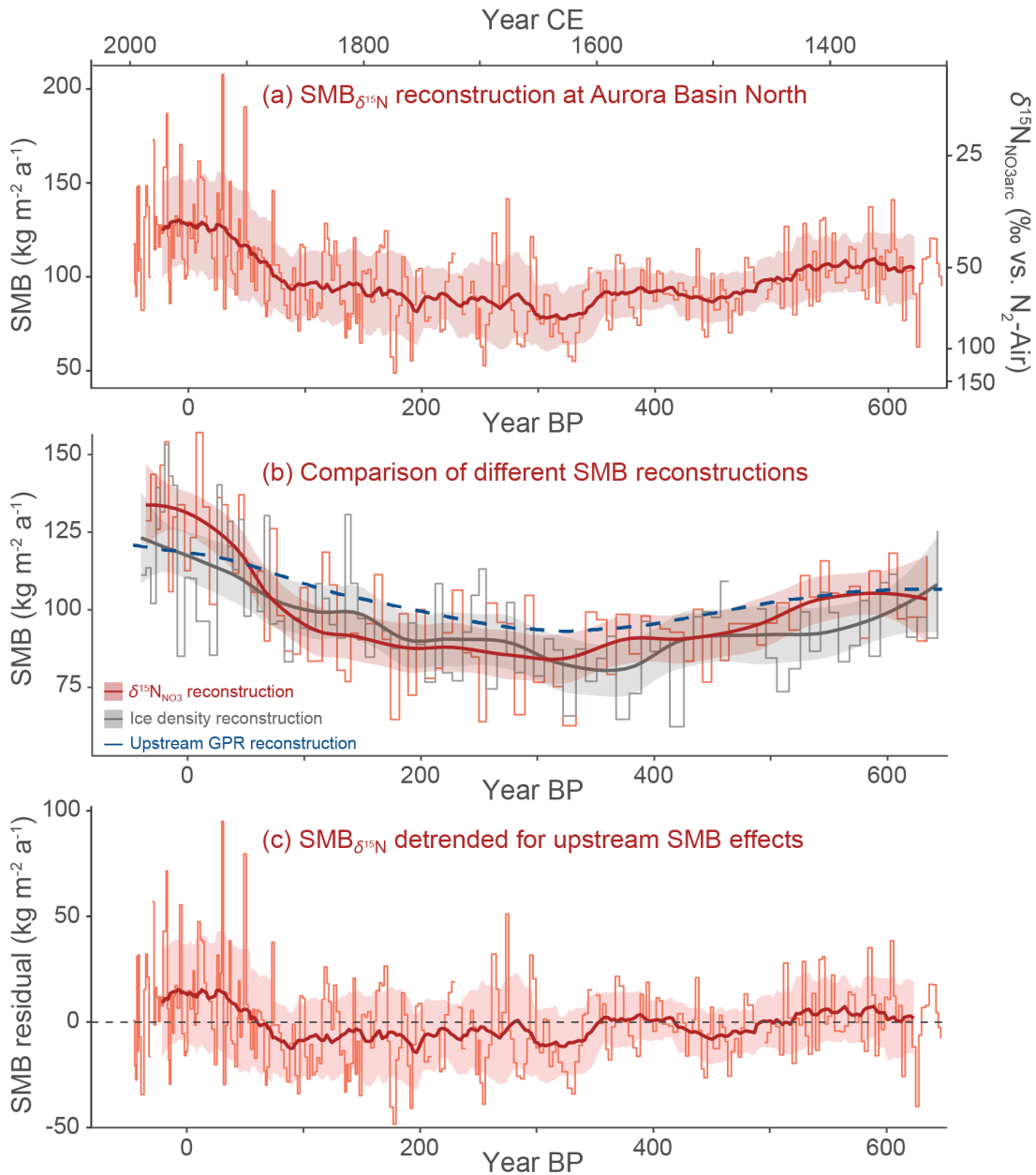


Figure 3. (a) Surface mass balance reconstruction for Aurora Basin North based on  $\delta^{15}N_{NO_3arc}$  data from the ABN1314-103 ice core. Reconstructed  $SMB_{\delta^{15}N}$  values are shown by the red stepped lines with the 50-yr running mean  $\pm 1\sigma$  overlaid as a darker thick line and shaded zone. (b) Comparison of SMBs reconstructed from  $\delta^{15}N_{NO_3}$  (red) with those from ice density (gray) and upstream GPR isochron depth<sup>39</sup>. The  $SMB_{\delta^{15}N}$  and  $SMB_{GPR}$  values were aggregated to match the 1-m resolution of the  $SMB_{density}$  data. For  $SMB_{\delta^{15}N}$  and  $SMB_{density}$ , smoothed LOESS curves are overlaid to more clearly show long-term patterns. (c)  $SMB_{\delta^{15}N}$  values after the upstream topographic impact on SMBs has been removed, with 50-yr running mean  $\pm 1\sigma$  values overlaid. The resulting residuals may better illustrate SMB variability due to climate change.

175 **Discussion: Validating the SMB<sub>δ15N</sub> proxy reconstruction**

We verified our new proxy's accuracy by comparing the SMB<sub>δ15N</sub> values with SMBs derived from the physical ice density (SMB<sub>density</sub>) measurements of the same core. For each 1-m core segment of ABN1314-103, we calculated a SMB<sub>density</sub> value by dividing the segment's mass (kg) by both its volume (m<sup>3</sup>) and the age difference between the top and bottom of the  
180 segment (a m<sup>-1</sup>). The SMB<sub>δ15N</sub> (aggregated to match the 1-m resolution) and SMB density share very similar mean values (100.8 vs. 98.0 kg m<sup>-2</sup> a<sup>-1</sup>, respectively) and total SMB ranges (62.0–157.3 vs. 61.7–153.4 kg m<sup>-2</sup> a<sup>-1</sup>, respectively), and the two SMB reconstructions have a similar pattern of variation with a moderate linear correlation (r = +0.46, p < 0.001, n = 90) (Figure 3b). This agreement in mean value, range, and variability strongly validates our  
185 SMB<sub>δ15N</sub> approach and the potential of δ<sup>15</sup>N<sub>NO3arc</sub> as an accurate proxy for paleoenvironmental change.

Interpreting the ABN1314-103 SMB profile is more complicated than for ice cores drilled at dome summits because the ice sheet at the ABN drilling site is flowing at a rate of 16.2 m a<sup>-1</sup>  
40. This means that the ice in ABN1314-103 actually fell as snow along a continuous 11.5 km  
190 transect upstream of the current ABN drilling site, with the oldest and deepest ice originating from the most distant upstream position. As a result, the δ<sup>15</sup>N<sub>NO3arc</sub> and core density have recorded any spatial SMB variability that existed along the upstream transect in addition to any SMB changes due to wetting or drying of the regional climate. Although overall elevation gain is small along the transect (<15 m), the region has abundant 0.5–1 m  
195 undulations in surface topography extending over horizontal extents of 3–10 km<sup>36</sup>. While the MAR's horizontal grid size (35 km) cannot resolve the SMB impact from these features, ground penetrating radar (GPR) performed along the upstream transect revealed that these

surface slope changes correlate with SMB variations of up to  $40 \text{ kg m}^{-2} \text{ a}^{-1}$  as determined by isochronic internal reflection horizons<sup>39,41</sup> (Figure 5). Although the long-term stability of such features is not well understood, the current surface features are still largely identifiable as buried horizons to depths below the deepest segment of ABN1314-103 with only steady horizontal offset due to ice flow.

By relating the upstream topographic-driven changes in SMB revealed by GPR to core depth through the horizontal ice flow rate and the core age-depth model<sup>39</sup>, we can determine the expected SMB signal due only to upstream surface topography ( $\text{SMB}_{\text{GPR}}$ ). We find that the general pattern of variability in  $\text{SMB}_{\text{GPR}}$  correlates very well with the patterns recorded in the  $\text{SMB}_{\delta^{15}\text{N}}$  ( $r = +0.74$ ) and  $\text{SMB}_{\text{density}}$  ( $r = +0.63$ ) records (Figure 3b). Thus, it appears that the primary SMB pattern preserved in ABN1314-103 is driven by upstream changes in surface slope, which is important for properly interpreting other environmental proxies contained in the ice and for understanding the local ice flow history.

### **Discussion: Extracting a climate-driven SMB record**

To examine whether a secondary signal related to climate change was also preserved, we removed the spatial impact of upstream topography by subtracting the  $\text{SMB}_{\text{GPR}}$  data from the  $\text{SMB}_{\delta^{15}\text{N}}$  record. After this “upstream effect detrending” and accounting for the small offset in mean SMB values ( $3.7 \text{ kg m}^{-2} \text{ a}^{-1}$ ), we find that the multi-decadal SMB values have been generally stable over the past 700 years (Figure 3c), with 50-yr running averages of the SMB never greater or less than  $15 \text{ kg m}^{-2} \text{ a}^{-1}$  from the detrended mean. These running averages suggest that drier conditions existed at ABN between 1600 and 1890 CE (partially corresponding to the Little Ice Age) and that precipitation has increased in the most recent 100–150 years. This is generally consistent with what has been observed at other East

Antarctic sites<sup>42–44</sup> and for Antarctica as a whole<sup>11</sup>, but we recognize that this pattern is similar to the upstream topographic effect and that it might also arise if the SMB<sub>GPR</sub> record is excessively smoothed relative to true topographic-driven SMB variability (perhaps by the GPR data processing).

On shorter timescales, SMBs frequently change by  $\approx 50 \text{ kg m}^{-2} \text{ a}^{-1}$  around a common mean within 10–20 year periods. This pattern likely reflects the high interannual snowfall variability expected at sites like ABN<sup>13</sup>. Located at the transition between the coast and the interior East Antarctic Plateau, annual snow accumulation at ABN is sensitive to chance intrusions of extreme precipitation events and atmospheric rivers<sup>45,46</sup>, and the observed sub-decadal SMB <sub>$\delta^{15}\text{N}$</sub>  variability may represent the frequency of their stochastic occurrence at the site. Additionally, small scale surface roughness features like sastrugi may affect hyperlocal SMB (i.e., the SMB at scales of  $< 1 \text{ m}$ ) through periods of enhanced accumulation and erosion as they migrate and evolve on the snow surface<sup>47–49</sup>. While the temporal evolution and possible life cycle cyclicity of surface roughness features are as yet poorly known, hyperlocal changes in SMB could also explain some of the short-term SMB variability observed in the ABN record if the sampling interval is shorter than the average duration of a surface feature at a given location.

#### **Discussion: Applied use and potential of the SMB <sub>$\delta^{15}\text{N}$</sub> proxy**

With over 8 million km<sup>2</sup> of Antarctica having a SMB between 40 and 200 kg m<sup>-2</sup> a<sup>-1</sup><sup>12</sup> and over 70% of the ice sheet area modeled to have  $\delta^{15}\text{N}_{\text{NO}_3}$  values markedly elevated by photolysis (Figure S6, Supplemental Text 4), the SMB <sub>$\delta^{15}\text{N}$</sub>  proxy holds great potential for vastly expanding our knowledge of Antarctic SMB variability over time and space.

Currently, regions with moderate SMBs have only a handful of sites with SMB records older

than 200 years, with the East Antarctic Plateau particularly poorly represented<sup>11</sup>. For ice coring projects in these regions, the SMB<sub>δ15N</sub> proxy will excel at capturing the local effects of strong winds, irregular surface topography, and high interannual snowfall variability better than water isotopic techniques while avoiding problems with layer thinning and density modeling that affect SMB<sub>density</sub> methods. As regional climate models still struggle to accurately simulate drifting snow and sublimation fluxes in the coast-to-plateau transition<sup>12</sup>, SMB<sub>δ15N</sub> can provide critical ground-based data for models predicting future contributions to sea level rise. The SMB<sub>δ15N</sub> proxy also holds particular value for helping constrain and validate models of upstream flow effects in research targeting ice streams and broad-scale glacial flow patterns.

Additionally, sampling for the SMB<sub>δ15N</sub> proxy can save valuable time and cost compared to existing alternatives in order to expand current records of modern SMBs. Obtaining new ground-based SMBs for sites without annually resolved layers requires either coring several meters to the increasingly buried Pinatubo volcanic horizon or repeated visits to newly installed stake transects. However, limited time and resources for research expeditions to remote areas precludes intensive SMB surveys with these methods. With the SMB<sub>δ15N</sub> proxy, a mean site SMB could be determined with only a series of shallow snow or firn samples extending deep enough into the archived zone to cover only a few seasonal cycles (much shallower than the Pinatubo horizon). After proper mixing, only ~0.3–1.0 kg would need to be kept, transported, and analyzed for each sample, which logistically allows for the rapid collection of robust SMB site means in many locations. On-site melting and NO<sub>3</sub><sup>-</sup> concentration could further reduce logistical requirements.

The SMB<sub>δ15N</sub> proxy promises to grow and adapt as studies on Antarctic NO<sub>3</sub><sup>-</sup> dynamics continue. Because the resolution of δ<sup>15</sup>N<sub>NO3arc</sub> sampling is limited only by the minimum

270 amount of  $\text{NO}_3^-$  needed for analysis, very finely-resolved  $\delta^{15}\text{N}_{\text{NO}_3\text{arc}}$  records can be obtained  
by increasing the mass of ice collected per depth unit (e.g., by specifically drilling whole  
cores or replicate cores for  $\text{NO}_3^-$  isotopes) and with advances in  $\text{NO}_3^-$  isotopic analysis  
expected in the near future<sup>50</sup>. This may allow for more precise multi-annual aggregations for  
SMB $_{\delta^{15}\text{N}}$  reconstructions and permit a deeper examination of subannual  $\text{NO}_3^-$  dynamics.

275 Finally, SMBs from parts of the West Antarctic ice sheet and the highest elevations of the  
northern Greenland ice sheet fall within the appropriate range for the SMB $_{\delta^{15}\text{N}}$  proxy, and  
additional field sampling at those locations may allow us to reconstruct SMBs by verifying or  
adapting the relationship defined here for regional use outside of East Antarctica. Given the  
great potential of the SMB $_{\delta^{15}\text{N}}$  proxy to advance our understanding of the Antarctic  
280 environment and its sensitivity to climate change, we strongly recommend that potential ice  
coring projects incorporate  $\text{NO}_3^-$  analyses into their planning and urge continued studies on  
Antarctic  $\text{NO}_3^-$  dynamics.

### **Acknowledgements:**

285 We express thanks to the following individuals for project assistance and data support: Sarah  
Albertin, Selin Bagci, Albane Barbero, Mathieu Casado, Armelle Crouzet, Vincent Favier,  
Elsa Gautier, Gaspard Jannot, Alexis Lamothe, Anaïs Orsi, Fred Parrenin, Holly Winton, and  
the overwintering crews at Concordia Station. We acknowledge the logistical support of  
IPEV for the French missions in Antarctica, the IPEV and PNRA colleagues and  
290 overwintering crews at Concordia Station, and the JARE54 traverse team for fieldwork  
assistance and access to the S80 site data. We thank the co-investigators for the ABN drilling  
project (Jérôme Chappellaz, Dorthe Dahl-Jensen, David Etheridge, Joe McConnell, Andrew  
Moy, Steven Phipps, Andrew Smith, Tessa Vance, Meredith Nation) and the French National

Center for Coring and Drilling (C2FN, funded by INSU) for critical drilling, logistic, and  
295 analytical support at ABN and other sites. Finally, we acknowledge the Glacioclim-SAMBA,  
ITASE, and IPICS 2kyr Array programs for SMB data, the Air-O-Sol facility at IGE for  
microbial culturing, and additional support from the MITACS Globalink program and JSPS-  
CNRS joint research program.

### **Funding:**

300 SCADI: European Horizon Marie Skłodowska-Curie individual fellowship 889508  
LabEx OSUG@2020 Investissements d'avenir: ANR10 LABX56  
EAIIST: ANR-16-CE01-0011-01  
BNP-Paribas Climate Initiative programs 1115 (CHICTABA), 1117 (CAPOXI 35-75), and  
1169 (EAIIST)  
305 CLIMCOR Equipex: ANR-11-EQPX-0009  
MEXT/JSPS KAKENHI: 20H0496

### **Author contributions:**

Conceptualization: PDA, JS, NC, MC  
Investigation: All authors  
310 Formal analysis: PDA, APMS, ELM  
Visualization: PDA, ELM  
Funding acquisition: PDA, JS, MC  
Writing – original draft: PDA, APMS, PC  
Writing – review & editing: All authors

315 The authors declare that they have no competing interests

**Data and materials availability:** Data and code are available for reviewers at  
doi:10.5281/zenodo.5793694. Data have been submitted to PANGAEA and are in review for  
publishing.

## 320 **Methods**

### ***Mathematical framework for $\delta^{15}\text{N}_{\text{NO}_3\text{arc}}$ and SMB relationships***

A linear relationship between  $\delta^{15}\text{N}_{\text{NO}_3\text{arc}}$  and the reciprocal of surface mass balance ( $\text{SMB}^{-1}$ )  
has been previously observed and reported in Antarctica<sup>17,34,26</sup>. Here, we mathematically  
illustrate how this relationship between  $\delta^{15}\text{N}_{\text{NO}_3\text{arc}}$  and SMB arises through photolysis of

325  $\text{NO}_3^-$ . We focus solely on the characteristics of  $\text{NO}_3^-$  contained within a given horizontal  
 plane of snow that is located at the snowpack surface at  $t = 0$ . We assume simplified sites  
 with a stable surface mass balance (*SMB*), clear sky conditions, no surface roughness, and no  
 significant compaction with burial in the photic zone. Any  $\text{NO}_3^-$  that is photolyzed is  
 immediately and permanently removed from the plane of snow, and  $\text{NO}_3^-$  recycling<sup>29,34</sup> is  
 330 assumed not to affect  $\text{NO}_3^-$  in the plane of snow during the burial process modeled here (i.e.,  
 after  $t = 0$ ).

*Defining the relationship between  $\delta^{15}\text{N}_{\text{NO}_3\text{arc}}$  and *SMB**

335 The time that it takes for a given horizontal plane of snow to be buried from the surface to a  
 particular depth  $z$  is determined by the *SMB* ( $\text{kg m}^{-2} \text{a}^{-1}$ , converted to  $\text{cm s}^{-1}$ ):

$$t_{(z)} = \frac{z}{\text{SMB}} \quad \text{Eq. (2)}$$

The concentration of  $\text{NO}_3^-$  within a plane of snow decays through time according to:

340

$$\frac{d[\text{NO}_3]}{dt} = -J_{(z)} [\text{NO}_3]_{(t)} \quad \text{Eq. (3)}$$

where  $J_{(z)}$  is the photolytic rate constant at a given depth defined as:

345

$$J_{(z)} = \sigma \phi I_{(z)} \quad \text{Eq. (4)}$$

where  $\sigma$  is the absorption cross section for  $\text{NO}_3^-$  photolysis ( $\text{cm}^2$ ),  $\phi$  is the quantum yield for  
 $\text{NO}_3^-$  photolysis ( $\text{molec photon}^{-1}$ ), and  $I_{(z)}$  is the actinic flux of ultraviolet irradiance ( $\text{photon}$   
 $\text{cm}^{-2} \text{s}^{-1} \text{nm}^{-1}$ ) integrated over wavelengths that can induce photolysis of  $\text{NO}_3^-$ . However, this  
 350 photolytic rate “constant” changes with depth because actinic flux exponentially decays with  
 depth as:

$$I_{(z)} = I_0 e^{\frac{-z}{z_e}} \quad \text{Eq. (5)}$$

355 where  $I_0$  is the initial actinic flux that strikes the snow surface and  $z_e$  is the  $e$ -folding depth  
 (cm) of the snowpack. Note that non-exponential decay of  $I$  in the top  $\sim 2$  cm of snowpack<sup>30</sup>  
 is simplified here by assuming the decay to be exponential from the snow surface. Equation  
 (3) can then be expressed as:

360

$$\frac{d[\text{NO}_3]}{dt} = -\sigma \phi I_0 e^{\frac{-z}{z_e}} [\text{NO}_3]_{(t)} \quad \text{Eq. (6)}$$

Through Eq. (2), we can rewrite Eq. (6) as:

$$\frac{d[NO_3]}{dt} = -\sigma \phi I_0 e^{\frac{-SMB t}{z_e}} [NO_3]_{(t)} \quad \text{Eq. (7)}$$

365

In order to determine the  $NO_3^-$  concentration at a given depth (i.e.,  $SMB \cdot t$ ), we derive:

$$\frac{d[NO_3]}{[NO_3]_{(t)}} = -\sigma \phi I_0 e^{\frac{-SMB t}{z_e}} dt \quad \text{Eq. (8)}$$

370

And integrate to produce:

$$\ln[NO_3]_{(t)} = \frac{\sigma \phi I_0 z_e e^{\frac{-SMB t}{z_e}}}{SMB} + C \quad \text{Eq. (9)}$$

Which simplifies to:

$$[NO_3]_{(t)} = e^C e^{\frac{\sigma \phi I_0 z_e e^{\frac{-SMB t}{z_e}}}{SMB}} \quad \text{Eq. (10)}$$

375

At  $t = 0$ ,  $[NO_3^-]_{(t)} = [NO_3^-]_0$  and therefore:

$$e^C = [NO_3]_0 e^{\frac{-\sigma \phi I_0 z_e}{SMB}} \quad \text{Eq. (11)}$$

380

And thus combining Eq. (10) and Eq. (11):

$$[NO_3]_{(t)} = [NO_3]_0 e^{\frac{-\sigma \phi I_0 z_e}{SMB}} e^{\frac{\sigma \phi I_0 z_e e^{\frac{-SMB t}{z_e}}}{SMB}} = [NO_3]_0 e^{\frac{\sigma \phi I_0 z_e (e^{\frac{-SMB t}{z_e}} - 1)}{SMB}} \quad \text{Eq. (12)}$$

385

According to Eq. (12), as time (i.e., burial depth) increases, the  $NO_3^-$  concentration will decrease. However, the rate of decrease will lessen over time as the value of  $SMB \cdot t$  approaches  $3z_e$ , and below the photic zone (i.e.,  $z > 3z_e$ ) the  $NO_3^-$  concentration is largely stable and equal to  $e^C$ .

390

Therefore, we can calculate the fraction of  $NO_3^-$  archived below the photic zone ( $f_{NO_3arc}$ ) as:

$$f_{NO_3arc} = \frac{e^C}{[NO_3]_0} = \frac{[NO_3]_0 e^{\frac{-\sigma \phi I_0 z_e}{SMB}}}{[NO_3]_0} = e^{\frac{-\sigma \phi I_0 z_e}{SMB}} \quad \text{Eq. (13)}$$

395

To determine the  $\delta^{15}N_{NO_3arc}$  of this  $NO_3^-$ , Rayleigh fractionation states that  $\delta^{15}N_{NO_3}$  can be calculated with the fractionation factor  $a$  by:

$$\ln(\delta^{15}N_{NO_3arc} + 1) = (a - 1) \ln(f_{NO_3arc}) + \ln(\delta^{15}N_{NO_3_0} + 1) \quad \text{Eq. (14)}$$

Through our prior calculation of  $f_{NO_3arc}$  in Eq. (13), we thus produce:

400

$$\ln(\delta^{15}N_{NO_3arc} + 1) = (a - 1) \frac{-\sigma \phi I_0 z_e}{SMB} + \ln(\delta^{15}N_{NO_3_0} + 1) \quad \text{Eq. (15)}$$

Because  $(a - 1)$  is negative for nitrogen during photolysis of  $NO_3^-$ <sup>21,22,31,51-53</sup> and the other parameters are positive, this means that  $\delta^{15}N_{NO_3arc}$  will vary linearly and positively with  $SMB^{-1}$  when other parameters are held constant or scale linearly with  $SMB^{-1}$ . We examine the

405 potential impacts of variability in these other parameters more thoroughly in Supplementary Text 1.

Based on modeling and field observations, SMB is the primary driver of change in  $\delta^{15}\text{N}_{\text{NO}_3\text{arc}}$  values. Thus, the non-SMB variables can be subsumed into two parameters  $A$  and  $B$  to function as linear regression coefficients, producing Eq. (1) of the main text:

410

$$\ln(\delta^{15}\text{N}_{\text{NO}_3\text{arc}} + 1) = \frac{A}{\text{SMB}} + B \quad \text{Eq. (1)}$$

The inverse function of Eq. (1) can be used as a transfer function to calculate an SMB based on a  $\delta^{15}\text{N}_{\text{NO}_3\text{arc}}$  value:

415

$$\frac{1}{\text{SMB}} = \frac{\ln(\delta^{15}\text{N}_{\text{NO}_3\text{arc}} + 1) - B}{A} \quad \text{Eq. (16)}$$

420 Finally, since  $\ln(x + 1) \approx x$  when  $x \approx 0$ , a simpler relationship of Eq. (15) can be approximated, in a form similar to that previously reported from field observations<sup>23,26,34</sup>:

$$\delta^{15}\text{N}_{\text{NO}_3\text{arc}} = (\alpha - 1) \frac{-\sigma \phi I_o z_e}{\text{SMB}} + \delta^{15}\text{N}_{\text{NO}_3_0} \quad \text{Eq. (17)}$$

### ***Snow sampling techniques***

425 The  $\delta^{15}\text{N}_{\text{NO}_3\text{arc}}$  values in our database are taken from a mix of previously reported values from Antarctic research traverses and values newly reported here (Figure 2). For all values, snow and ice containing  $\text{NO}_3^-$  was sampled in the field in one of three techniques: 1) 1–2 m deep snow pit with continuous sampling at regular intervals from top to bottom, 2) single sample taken of a well-mixed 5–10 cm layer around the 1-m depth layer, and 3) drilled core

430 later cut at desired intervals. Since current  $\text{NO}_3^-$  isotopic analysis requires 50–150 nmol of  $\text{NO}_3^-$ , 0.25–1.50 kg of snow or ice per sample<sup>19,21</sup> are gathered to ensure a sufficient amount of  $\text{NO}_3^-$ . Generally, the multiple samples produced by the snow pit technique offers the best and most flexible results, but the 1-m depth layer technique is valuable for quick sampling during limited stops, and cores are necessary to collect samples deeper than  $\approx 5$  m.

435

### ***Laboratory analyses***

For  $\delta^{15}\text{N}_{\text{NO}_3\text{arc}}$  results included in our database that have been previously reported, readers are directed to the original papers for specific analytical and sampling techniques. For the

$\delta^{15}\text{N}_{\text{NO}_3\text{arc}}$  data newly reported here, snow and ice samples were collected into clean sealed plastic bags or tubs and stored frozen until melted at room temperature for analysis. The  $\text{NO}_3^-$  mass fraction ( $\omega(\text{NO}_3^-)$ ) was determined on aliquots by either a colorimetric method or ion chromatography with detection limits  $< 0.5 \text{ ng g}^{-1}$  and precision of  $< 3\%$ <sup>21,22</sup>. The remaining melted samples were passed through an anionic exchange resin (Bio-Rad™ AG 1-X8, chloride form), and the resulting trapped  $\text{NO}_3^-$  was eluted with 10 ml of NaCl 1 M solution.

Isotopic analysis occurred at IGE-CNRS, Grenoble, France, where  $\text{NO}_3^-$  in these samples was converted to  $\text{N}_2\text{O}$  with the denitrifying bacteria *Pseudomonas aureofaciens* (lacking nitrous oxide reductase), thermally decomposed into  $\text{O}_2$  and  $\text{N}_2$  on a  $900^\circ \text{C}$  gold surface, and separated by gas chromatography with a GasBench II™. Oxygen and nitrogen isotopic ratios were then measured on a Thermo Finnigan™ MAT 253 mass spectrometer<sup>54-57</sup>. Isotopic effects from this analysis were corrected as described by Morin et al. (2009) and Frey et al. (2009), using the international reference materials USGS 32, USGS 34, and USGS 35 with ultrapure Dome C water used for standards and samples throughout the analyses to account for potential oxygen isotopic exchanges. Results are reported relative to Vienna Standard Mean Ocean Water (V-SMOW) for oxygen isotopes<sup>58</sup> and  $\text{N}_2$ -Air for nitrogen isotopes<sup>59</sup>.

For snow pits with multiple sequential  $\delta^{15}\text{N}_{\text{NO}_3\text{arc}}$  values, a single  $\delta^{15}\text{N}_{\text{NO}_3\text{arc}}$  value was calculated as the aggregate of samples 30+ cm deep, weighted by the relative mass of  $\text{NO}_3^-$  per sample. Although the photic zone boundary can extend lower than 30 cm at some sites<sup>29,30</sup>, this cutoff was deemed an acceptable compromise to include more data from pits that stopped at 50 cm depth as the great majority of photolysis will have occurred within the top 30 cm due to exponential decay of actinic flux and  $\omega(\text{NO}_3^-)$  with depth. Exceptions to this were made for three coastal pits from Cap Prud'homme (weighted-means of 3+ cm samples), where high accumulation greatly reduces photolytic impact, higher snow impurities reduce the photic zone depth, and a broader aggregation is necessary to smooth seasonal cycles.

Additionally, two pits from Dronning Maud Land were aggregated with 15+ cm samples based on shallow  $3z_e$  values (2–5 cm) calculated on site during snow pit sampling<sup>29</sup>. For cores included in our database, a single  $\delta^{15}\text{N}_{\text{NO}_3\text{arc}}$  value was calculated as the isotopic mean of samples extending from present back to no earlier than 1800 CE.

Noro et al. (2018) reported  $\delta^{15}\text{N}_{\text{NO}_3}$  values for 16 pits along the JARE54 and JARE57 transects, but the sampling methodology for these pits took a single well-mixed sample of the entire pit depth which included the entire photic zone. In order to estimate the  $\delta^{15}\text{N}_{\text{NO}_3\text{arc}}$  values of these sites (i.e., the value as if the photic zone snow had been excluded), we applied a correction factor calculated using data from other pits in our database that were taken on two similar transects spanning from the coast to other interior domes (Dome A and Dome C) of East Antarctica<sup>22,23</sup>. Because each of the pits on the Dome A and Dome C transects were continuously sampled at discrete intervals from the surface to a point below the photic zone, we calculated different weighted-mean  $\delta^{15}\text{N}_{\text{NO}_3}$  values for selected depth spans that matched the three extents of the JARE pits: 0–30 cm, 0–50 cm, and 0–80 cm. Corrective factors were calculated through the linear regression of  $\delta^{15}\text{N}_{\text{NO}_3\text{arc}}$  vs.  $\delta^{15}\text{N}_{\text{NO}_3.X}$  from Dome A/Dome C transect pits (where  $\delta^{15}\text{N}_{\text{NO}_3\text{arc}}$  is our database's  $\delta^{15}\text{N}_{\text{NO}_3}$  value from the archived zone and  $\delta^{15}\text{N}_{\text{NO}_3.X}$  is the weighted-mean value of samples from the surface to depth  $x$ : 30, 50, or 80 cm) and applied to the JARE pit data through the appropriate depth correction (Table 1, 2). Corrections were not made for JARE samples where  $\delta^{15}\text{N}_{\text{NO}_3} < 0 \text{ ‰}$ , as these low  $\delta^{15}\text{N}_{\text{NO}_3}$  values strongly suggest that photolysis was not a significant factor at these coastal sites, and photic zone corrections were thus not warranted.

Table 1. Linear regressions of  $\delta^{15}\text{N}_{\text{NO}_3\text{arc}}$  vs.  $\delta^{15}\text{N}_{\text{NO}_3.X}$  (where X is 30, 50, or 80 cm) calculated from non-JARE pit data in the  $\delta^{15}\text{N}_{\text{NO}_3}$  database.

Depth correction	Slope (‰ / ‰)	Intercept (‰)	r <sup>2</sup>
0–30 cm	1.9±0.1	-2.4±11.3	0.89
0–50 cm	1.6±0.1	-1.7±8.2	0.94
0–80 cm	1.5±0.1	-0.9±7.8	0.94

490

Table 2. The  $\delta^{15}\text{N}_{\text{NO}_3}$  values for JARE sites included in our database as originally reported by Noro et al. (2018) and the  $\delta^{15}\text{N}_{\text{NO}_3\text{arc}}$  values corrected here to account for photic zone snow included in the original samples. Samples with original  $\delta^{15}\text{N}_{\text{NO}_3}$  values  $< 0$  ‰ (italicized) were not corrected.

JARE site	Depth (cm)	Original $\delta^{15}\text{N}_{\text{NO}_3}$ (‰)	Corrected $\delta^{15}\text{N}_{\text{NO}_3\text{arc}}$ (‰)
Z2	0–80	20.6	30.8
IM0	0–50	25.7	40.3
NMD304	0–50	41.1	65.4
MD590	0–50	83.5	134.7
DF1	0–30	127.3	236.5
NDF	0–30	111.7	207.2
Plateau S	0–30	165.5	308.1
S80	0–30	90.7	167.8
Fuji Pass	0–30	74.3	137.0
DF2	0–30	118.6	220.1
<i>S30</i>	<i>0–50</i>	<i>-19.0</i>	<i>-19.0</i>
<i>H42</i>	<i>0–50</i>	<i>-6.6</i>	<i>-6.6</i>
<i>H68</i>	<i>0–50</i>	<i>-14.5</i>	<i>-14.5</i>
<i>H88</i>	<i>0–50</i>	<i>-19.4</i>	<i>-19.4</i>
<i>H108</i>	<i>0–50</i>	<i>-6.4</i>	<i>-6.4</i>
H128	0–50	14.1	21.3

### ***SMB data***

495

In our database, 74  $\delta^{15}\text{N}_{\text{NO}_3\text{arc}}$  samples are represented by 51 unique direct ground measurements of SMB ( $\text{SMB}_{\text{ground}}$ ) values observed at or near the  $\text{NO}_3^-$  sampling site, with the numerical discrepancy due to some sites having replicate  $\delta^{15}\text{N}_{\text{NO}_3\text{arc}}$  samples. These previously reported  $\text{SMB}_{\text{ground}}$  values were determined by measuring the change in surface height on established stakes or poles, by measuring the mass between known volcanic or radioactivity horizons in an ice core, or by ground penetrating radar (GPR) identification of dated horizons<sup>10,22,23,60–67</sup>.

500

Regional climate models can be used to estimate modern SMB rates for sites lacking ground observations<sup>7,12</sup>, and we used the Modèle Atmosphérique Régional (MAR) version 3.6.4 with European Centre for Medium-Range Weather Forecasts “Interim” re-analysis data (ERA-interim) data as applied by Agosta et al. (2019) to model mean annual SMBs at all database sites for the period 1979–2017<sup>12</sup>. Because the MAR overestimates SMBs at higher and more interior sites of the East Antarctic plateau<sup>68</sup>, we calculated a correction factor through linear

505

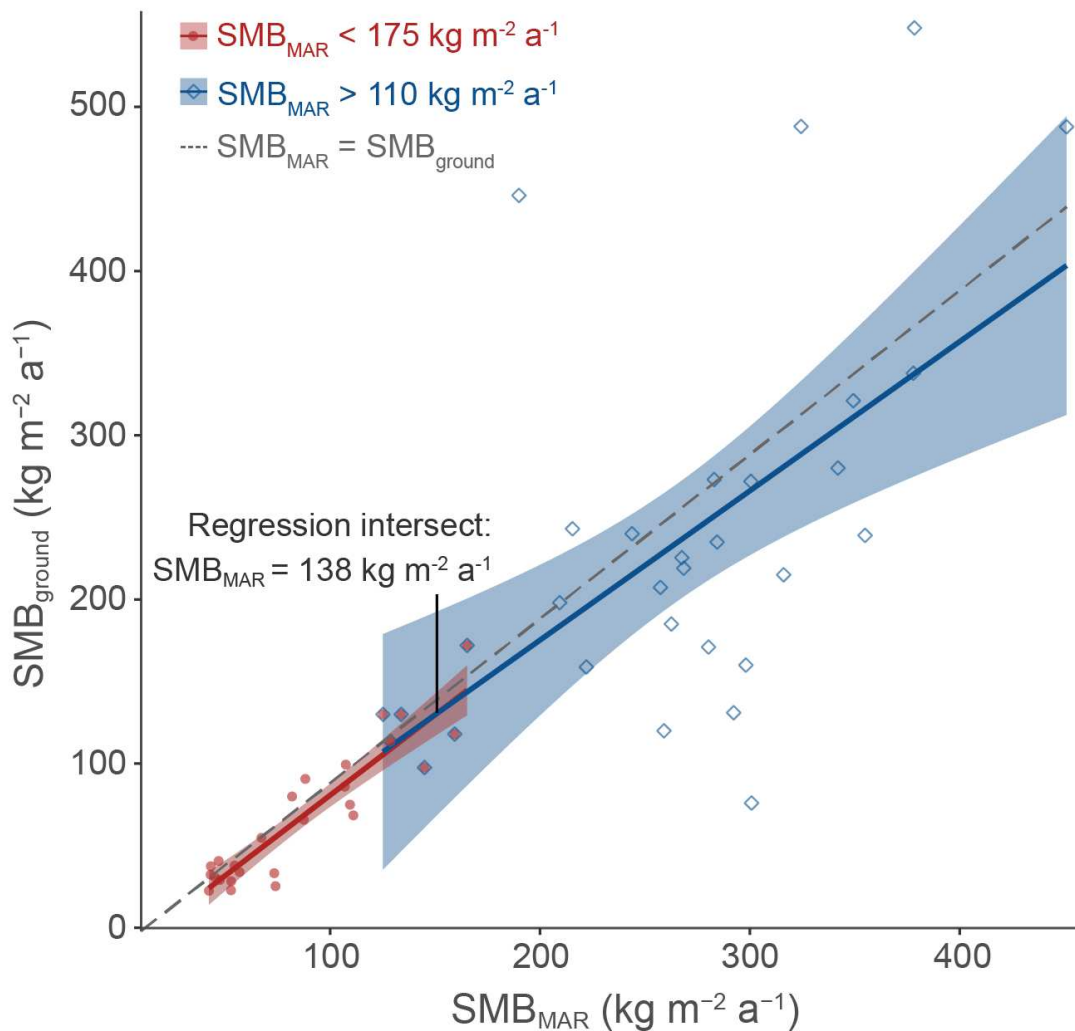
regressions of  $SMB_{ground}$  vs. MAR-estimated SMBs ( $SMB_{MAR}$ ) for our 51 sites that have both values (Table 3, Figure 4). This correction was applied to all original MAR estimates to produce “adjusted-MAR” SMBs ( $SMB_{adjMAR}$ ) that match more closely with ground observations.

510

Table 3. A list of all sampling sites that have a  $SMB_{ground}$  observation with corresponding values of original  $SMB_{MAR}$  and  $SMB_{adjMAR}$  (Figure 4). The difference between the  $SMB_{adjMAR}$  and  $SMB_{MAR}$  values is given in the final column.

Site	$SMB_{ground}$ ( $kg\ m^{-2}\ a^{-1}$ )	$SMB_{MAR}$ ( $kg\ m^{-2}\ a^{-1}$ )	$SMB_{adjMAR}$ ( $kg\ m^{-2}\ a^{-1}$ )	$SMB_{adjMAR} - SMB_{MAR}$ ( $kg\ m^{-2}\ a^{-1}$ )	$SMB_{adjMAR} / SMB_{MAR}$
Vostok	22.6	30.4	24.1	-6.3	0.79
DomeA	22.9	40.9	34.4	-6.5	0.84
ZtoA-P6	25.4	62.1	55.2	-6.9	0.89
DomeC	28.4	41.0	34.5	-6.5	0.84
DomeF	29.2	35.6	29.2	-6.4	0.82
NDF	30.9	33.2	26.8	-6.4	0.81
Plateau S	32.4	31.2	24.8	-6.4	0.79
ZtoA-P5	33.3	61.5	54.6	-6.9	0.89
preeaiist.18	34.0	47.8	41.1	-6.7	0.86
S80Jare	37.5	31.3	24.9	-6.4	0.80
MD590	37.9	42.6	36.0	-6.6	0.85
Fuji Pass	40.7	35.0	28.6	-6.4	0.82
ZtoA-P4	54.8	55.4	48.6	-6.8	0.88
NMD304	65.8	75.6	68.4	-7.2	0.90
IM0	68.5	99.2	91.6	-7.6	0.92
Kohnen	75.0	97.6	90.0	-7.6	0.92
posteiist.asuma05	76.0	288.9	266.9	-22.0	0.92
preeaiist.15	80.0	70.0	62.9	-7.1	0.90
preeaiist.13	86.0	95.1	87.5	-7.6	0.92
ZtoA-P3	90.7	76.3	69.1	-7.2	0.91
CPH.D5	97.6	139.7	124.8	-8.3	0.89
ZtoA-P2	99.4	95.6	88.0	-7.6	0.92
Z2	113.5	116.9	108.9	-8.0	0.93
posteiist.stop36	118.0	147.5	138.3	-9.2	0.94
CPH.D24	120.0	247.2	228.9	-18.3	0.93
preeaiist.12	130.0	113.3	105.4	-7.9	0.93
ABN	130.0	122.0	113.9	-8.1	0.93
posteiist.asuma06	131.0	280.4	259.1	-21.3	0.92
H128	158.8	210.2	195.3	-14.9	0.93
preeaiist.06	160.0	286.2	264.4	-21.8	0.92
preeaiist.07	171.0	269.5	249.2	-20.3	0.92
ZtoA-P1	172.0	153.4	143.7	-9.7	0.94
H108	185.0	250.7	232.1	-18.6	0.93
preeaiist.09	198.0	201.0	186.9	-14.1	0.93
H88	207.3	245.5	227.4	-18.1	0.93
posteiist.asuma04	215.0	304.2	280.8	-23.4	0.92
posteiist.asuma09	219.0	256.6	237.5	-19.1	0.93
H68	225.4	255.7	236.7	-19.0	0.93
H42	234.9	272.5	251.9	-20.6	0.92
posteiist.asuma02	239.0	343.0	316.0	-27.0	0.92
posteiist.asuma10	240.0	232.0	215.1	-16.9	0.93

posteiist.asuma11	243.0	203.6	189.3	-14.3	0.93
S30-JARE	271.9	288.6	266.6	-22.0	0.92
posteiist.asuma07	273.0	271.1	250.7	-20.4	0.92
preeiist.04	280.0	330.1	304.3	-25.8	0.92
posteiist.asuma01	321.0	337.4	310.9	-26.5	0.92
preeiist.03	337.7	366.0	337.0	-29.0	0.92
cph.d17	446.0	178.1	166.1	-12.0	0.93
preeiist.02	487.8	439.0	403.3	-35.7	0.92
asuma.2016.2	488.0	312.5	288.3	-24.2	0.92
asuma.2016.1	548.0	366.5	337.4	-29.1	0.92



515 Figure 4. Linear regressions of  $SMB_{ground}$  versus  $SMB_{MAR}$  for the period 1979–2017 at the 51 sites with  $SMB_{ground}$  observations, with 95% confidence intervals of the regressions shaded. Sites are subset for two overlapping regressions that intersect at (138, 130). These linear regressions were applied to the  $SMB_{MAR}$  values for all sampling sites to produce the  $SMB_{adjMAR}$  used in analyses. The dashed line represents a slope of 1 (i.e., if the  $SMB_{MAR}$  perfectly matched the  $SMB_{ground}$ ).

520 A linear regression was calculated for two overlapping subsets of sites: one for the set of well-grouped sites where the  $SMB_{MAR}$  is  $< 175\ kg\ m^{-2}\ a^{-1}$  and another for all sites where  $SMB_{MAR}$  is  $> 110\ kg\ m^{-2}\ a^{-1}$ . This first regression is tightly constrained ( $SMB_{ground} = 1.0 \pm$

0.1 × SMB<sub>MAR</sub> - 5.8 ± 7.1, r<sup>2</sup> = 0.84), and it performs well to better align the SMB<sub>MAR</sub> estimates with the SMB<sub>ground</sub> values at low SMB sites. The second regression covers samples with where some differences between SMB<sub>MAR</sub> and SMB<sub>ground</sub> are very large, particularly at lower elevation sites where intense aeolian erosion and deposition can produce highly variable local SMB rates that are difficult to accurately model<sup>12,13</sup>. As a result, this regression is weaker (SMB<sub>ground</sub> = 0.9 ± 0.2 × SMB<sub>MAR</sub> + 4.2 ± 57.9, r<sup>2</sup> = 0.35) than the first regression, but we apply it while acknowledging the possibility of wide deviations. The two regressions intersect at (SMB<sub>MAR</sub> = 138 kg m<sup>-2</sup> a<sup>-1</sup>, SMB<sub>ground</sub> = 130 kg m<sup>-2</sup> a<sup>-1</sup>), and thus SMB<sub>adjMAR</sub> values were calculated by applying the first regression to all sites where SMB<sub>MAR</sub> ≤ 138 kg m<sup>-2</sup> a<sup>-1</sup> and applying the second regression to all sites where SMB<sub>MAR</sub> > 138 kg m<sup>-2</sup> a<sup>-1</sup>. We constructed our final primary SMB dataset for the analysis of δ<sup>15</sup>N<sub>NO3arc</sub> samples by using the best quality SMB data for each site: SMB<sub>ground</sub> if available and SMB<sub>adjMAR</sub> otherwise.

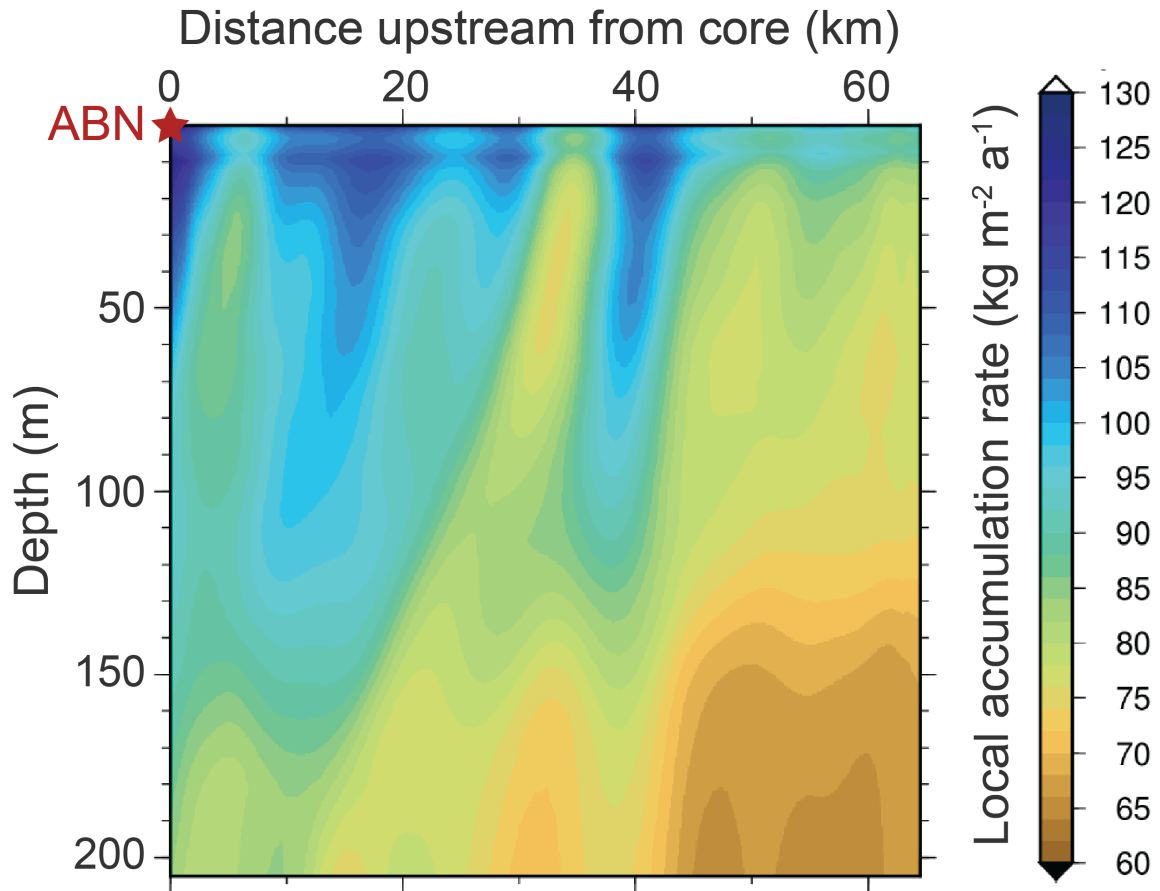
### ***Transfer function and SMB reconstruction***

We modeled linear relationships between ln(δ<sup>15</sup>N<sub>NO3</sub> + 1) and SMB<sup>-1</sup> based on Eq. (15) using previously reported parameter values to compare our theoretical framework to field results and to better understand the sensitivity of the relationships to photolytic and fractionation factors (Supplementary Text 1). To determine the coefficients in Eq. (1) from our field data, we performed linear regressions using all database samples and the primary SMB dataset. Additional regressions (Supplementary Text 2) were performed for subsets of the database based on SMB type (SMB<sub>ground</sub> vs. SMB<sub>adjMAR</sub>). With regression coefficients determined for Eq. (1), we modeled the spatial distribution of δ<sup>15</sup>N<sub>NO3arc</sub> values across Antarctica using gridded mean SMBs (MAR-ERA-interim, 1979–2015) at a 35 km resolution<sup>12</sup> that were converted to SMB<sub>adjMAR</sub> as previously described.

For reconstructing the ABN  $\text{SMB}_{\delta^{15}\text{N}}$  history, the ABN1314-103 ice core was cut into 0.33 m samples from 5 to 103 m, and these were processed for  $\text{NO}_3^-$  isotopes in 2016 as previously described. We applied an annually-resolved age model (ALC01112018) based on seasonal  
550 ion and water isotope cycles and constrained by volcanic horizons that was originally developed for a longer core also taken at ABN. Each 1 m ice core segment was individually weighed prior to cutting, and the mass and volume were used to calculate a SMB profile based on dated ice density changes ( $\text{SMB}_{\text{density}}$ ).

To determine past topographical effects on SMBs, a MALA GPR device towing a RTA  
555 antenna on the surface (50 MHz out, 100 MHz in) was operated for a 65 km transect upstream of the coring site as part of the 2013–2014 campaign. Radar was triggered every 2 seconds (i.e., every 6–7 m along the transect) with a recording time window of 3000 nanoseconds that captured returns down to 300 m depth. After postprocessing<sup>41</sup>, isochronic internal reflecting horizons were identified to 220 m depth, digitized with ReflexW software,  
560 and dated by connecting to the ALC01112018 age-depth model. Using a density profile taken from a longer ice core simultaneously drilled at ABN, 2D fields (depth by transect distance) were calculated for age, mean accumulation rate, and local accumulation rate. The mean accumulation rate to the most shallow reflecting horizon was taken as the upstream topographical effect on SMBs (i.e.,  $\text{SMB}_{\text{GPR}}$ ).

565 Statistical analyses, regressions, SMB reconstructions, visualizations, and other statistical analyses were performed using the R programming language with packages *ggplot2*, *RColorBrewer*, *gridExtra*, *cowplot*, and *tidyverse*.



570

Figure 5. Local accumulation rate variability with depth along the upstream ABN transect determined from GPR identification of isochronic internal reflective horizons. Accumulation rates have an original depth resolution of 0.5 m which is smoothed through a moving age-depth average with a cosine weighting window to reduce isochron artifacts<sup>41</sup>.

1. Fretwell, P. *et al.* Bedmap2: improved ice bed, surface and thickness datasets for Antarctica. *The Cryosphere* **7**, 375–393 (2013).
2. Juckes, M. N., James, I. N. & Blackburn, M. The influence of Antarctica on the momentum budget of the southern extratropics. *Quarterly Journal of the Royal Meteorological Society* **120**, 1017–1044 (1994).
- 580 3. M.R. van den Broeke. On the role of Antarctica as heat sink for the global atmosphere. *J. Phys. IV France* **121**, 115–124 (2004).
4. Bronselaer, B. *et al.* Change in future climate due to Antarctic meltwater. *Nature* **564**, 53–58 (2018).
5. Starr, A. *et al.* Antarctic icebergs reorganize ocean circulation during Pleistocene glacials. *Nature* **589**, 236–241 (2021).
- 585 6. IPCC. Climate Change 2014: Synthesis Report. Contribution of Working Groups I, II and III to the Fifth Assessment Report of the Intergovernmental Panel on Climate Change [Core Writing Team, R.K. Pachauri and L.A. Meyer (eds.)]. 151 (2014).
7. Shepherd, A. *et al.* Mass balance of the Antarctic Ice Sheet from 1992 to 2017. *Nature* **558**, 219–222 (2018).
- 590 8. Martín-Español, A. *et al.* Spatial and temporal Antarctic Ice Sheet mass trends, glacio-isostatic adjustment, and surface processes from a joint inversion of satellite altimeter, gravity, and GPS data. *Journal of Geophysical Research: Earth Surface* **121**, 182–200 (2016).
9. Stauffer, B., Flückiger, J., Wolff, E. & Barnes, P. The EPICA deep ice cores: first results and perspectives. *Annals of Glaciology* **39**, 93–100 (2004).
- 595 10. Parrenin, F. *et al.* 1-D-ice flow modelling at EPICA Dome C and Dome Fuji, East Antarctica. *Clim. Past* **3**, 243–259 (2007).
11. Thomas, E. R. *et al.* Regional Antarctic snow accumulation over the past 1000 years. *Clim. Past* **13**, 1491–1513 (2017).
12. Agosta, C. *et al.* Estimation of the Antarctic surface mass balance using the regional climate model MAR (1979–2015) and identification of dominant processes. *The Cryosphere* **13**, 281–296 (2019).
- 600 13. Agosta, C. *et al.* A 40-year accumulation dataset for Adelie Land, Antarctica and its application for model validation. *Climate Dynamics* **38**, 75–86 (2012).
14. Gallée, H. *et al.* Transport of Snow by the Wind: A Comparison Between Observations in Adélie Land, Antarctica, and Simulations Made with the Regional Climate Model MAR. *Boundary-Layer Meteorology* **146**, 133–147 (2013).
- 605

15. Vimeux, F., Cuffey, K. M. & Jouzel, J. New insights into Southern Hemisphere temperature changes from Vostok ice cores using deuterium excess correction. *Earth and Planetary Science Letters* **203**, 829–843 (2002).
16. Cauquoin, A. *et al.* Comparing past accumulation rate reconstructions in East Antarctic ice cores using <sup>10</sup>Be, water isotopes and CMIP5-PMIP3 models. *Clim. Past* **11**, 355–367 (2015).
- 610 17. Freyer, H. D., Kobel, K., Delmas, R. J., Kley, D. & Legrand, M. R. First results of <sup>15</sup>N/<sup>14</sup>N ratios in nitrate from alpine and polar ice cores. *Tellus B* **48**, 93–105 (1996).
18. Legrand, M., Wolff, E., Wagenbach, D. & Jacka, T. Antarctic aerosol and snowfall chemistry: implications for deep Antarctic ice-core chemistry. *Annals of Glaciology, Vol 29, 1999* **29**, 66–72 (1999).
- 615 19. Wolff, E. Nitrate in Polar Ice. in *Ice Core Studies of Global Biogeochemical Cycles* (Springer-Verlag, 1995).
20. Röthlisberger, R. *et al.* Nitrate in Greenland and Antarctic ice cores: a detailed description of post-depositional processes. *Annals of Glaciology* **35**, 209–216 (2002).
21. Frey, M., Savarino, J., Morin, S., Erbland, J. & Martins, J. Photolysis imprint in the nitrate stable isotope signal in snow and atmosphere of East Antarctica and implications for reactive nitrogen cycling. *Atmospheric Chemistry and Physics* **9**, 8681–8696 (2009).
- 620 22. Erbland, J. *et al.* Air-snow transfer of nitrate on the East Antarctic Plateau - Part 1: Isotopic evidence for a photolytically driven dynamic equilibrium in summer. *Atmospheric Chemistry and Physics* **13**, 6403–6419 (2013).
- 625 23. Shi, G. *et al.* Investigation of post-depositional processing of nitrate in East Antarctic snow: isotopic constraints on photolytic loss, re-oxidation, and source inputs. *Atmospheric Chemistry and Physics* **15**, 9435–9453 (2015).
24. Grannas, A. *et al.* An overview of snow photochemistry: evidence, mechanisms and impacts. *Atmospheric Chemistry and Physics* **7**, 4329–4373 (2007).
- 630 25. Berhanu, T. *et al.* Laboratory study of nitrate photolysis in Antarctic snow. II. Isotopic effects and wavelength dependence. *Journal of Chemical Physics* **140**, (2014).
26. Noro, K. *et al.* Spatial variation of isotopic compositions of snowpack nitrate related to post-depositional processes in eastern Dronning Maud Land, East Antarctica. *Geochemical Journal* **52**, e7–e14 (2018).
- 635 27. Shi, G. *et al.* Isotope fractionation of nitrate during volatilization in snow: A field investigation in Antarctica. *Geophysical Research Letters* **46**, 3287–3297 (2019).

28. Noro, K. & Takenaka, N. Post-depositional loss of nitrate and chloride in Antarctic snow by photolysis and sublimation: a field investigation. *POLAR* **39**, (2020).
29. Winton, V. H. L. *et al.* Deposition, recycling, and archival of nitrate stable isotopes between the air–snow interface: comparison between Dronning Maud Land and Dome C, Antarctica. *Atmos. Chem. Phys.* **20**, 5861–5885 (2020).
- 640 30. Zatko, M. C. *et al.* The influence of snow grain size and impurities on the vertical profiles of actinic flux and associated NO<sub>x</sub> emissions on the Antarctic and Greenland ice sheets. *Atmos. Chem. Phys.* **13**, 3547–3567 (2013).
31. Zatko, M., Geng, L., Alexander, B., Sofen, E. & Klein, K. The impact of snow nitrate photolysis on  
645 boundary layer chemistry and the recycling and redistribution of reactive nitrogen across Antarctica and Greenland in a global chemical transport model. *Atmos. Chem. Phys.* **16**, 2819–2842 (2016).
32. France, J. L. *et al.* Snow optical properties at Dome C (Concordia), Antarctica; implications for snow emissions and snow chemistry of reactive nitrogen. *Atmos. Chem. Phys.* **11**, 9787–9801 (2011).
33. Wolff, E., Jones, A., Martin, T. & Grenfell, T. Modelling photochemical NO<sub>x</sub> production and nitrate loss  
650 in the upper snowpack of Antarctica. *Geophysical Research Letters* **29**, (2002).
34. Erbland, J. *et al.* Air-snow transfer of nitrate on the East Antarctic Plateau - Part 2: An isotopic model for the interpretation of deep ice-core records. *Atmospheric Chemistry and Physics* **15**, 12079–12113 (2015).
35. Jiang, S. *et al.* Nitrate preservation in snow at Dome A, East Antarctica from ice core concentration and isotope records. *Atmospheric Environment* **213**, 405–412 (2019).
- 655 36. Howat, I. M., Porter, C., Smith, B. E., Noh, M.-J. & Morin, P. The Reference Elevation Model of Antarctica. *The Cryosphere* **13**, 665–674 (2019).
37. Hui, F. *et al.* Mapping blue-ice areas in Antarctica using ETM+ and MODIS data. *Annals of Glaciology* **55**, 129–137 (2014).
38. Savarino, J., Kaiser, J., Morin, S., Sigman, D. & Thiemens, M. Nitrogen and oxygen isotopic constraints on  
660 the origin of atmospheric nitrate in coastal Antarctica. *Atmospheric Chemistry and Physics* **7**, 1925–1945 (2007).
39. Servettaz, A., Landais, A. & Orsi, A. Two thousand years of temperature variability on the lower East Antarctic Plateau inferred from the analysis of stable isotopes of water and inert gases in the Aurora Basin North ice core. (Université Paris-Saclay, 2021).

- 665 40. Mouginot, J., Rignot, E. & Scheuchl, B. Continent-wide, interferometric SAR phase, mapping of Antarctic ice velocity. *Geophysical Research Letters* **46**, 9710–9718 (2019).
41. Le Meur, E. *et al.* Spatial and temporal distributions of surface mass balance between Concordia and Vostok stations, Antarctica, from combined radar and ice core data: first results and detailed error analysis. *The Cryosphere* **12**, 1831–1850 (2018).
- 670 42. Stenni, B. *et al.* Eight centuries of volcanic signal and climate change at Talos Dome (East Antarctica). *J. Geophys. Res.-Atmos.* **107**, 13 (2002).
43. Frezzotti, M., Scarchilli, C., Becagli, S., Proposito, M. & Urbini, S. A synthesis of the Antarctic surface mass balance during the last 800 yr. *The Cryosphere* **7**, 303–319 (2013).
44. Urbini, S. *et al.* Historical behaviour of Dome C and Talos Dome (East Antarctica) as investigated by snow accumulation and ice velocity measurements. *Global and Planetary Change* **60**, 576–588 (2008).
- 675 45. Wille, J. D. *et al.* Antarctic atmospheric river climatology and precipitation impacts. *Journal of Geophysical Research: Atmospheres* **126**, (2021).
46. Turner, J. *et al.* The Dominant Role of Extreme Precipitation Events in Antarctic Snowfall Variability. *Geophysical Research Letters* **46**, 3502–3511 (2019).
- 680 47. Frezzotti, M., Gandolfi, S., Marca, F. L. & Urbini, S. Snow dunes and glazed surfaces in Antarctica: new field and remote-sensing data. *Annals of Glaciology* **34**, 81–88 (2002).
48. Libois, Q., Picard, G., Arnaud, L., Morin, S. & Brun, E. Modeling the impact of snow drift on the decameter-scale variability of snow properties on the Antarctic Plateau. *Journal of Geophysical Research: Atmospheres* **119**, 11662–11681 (2014).
- 685 49. Picard, G., Arnaud, L., Caneill, R., Lefebvre, E. & Lamare, M. Observation of the process of snow accumulation on the Antarctic Plateau by time lapse laser scanning. *The Cryosphere* **13**, 1983–1999 (2019).
50. Neubauer, C. *et al.* Stable isotope analysis of intact oxyanions using electrospray quadrupole-orbitrap mass spectrometry. *Anal. Chem.* **92**, 3077–3085 (2020).
51. Meusinger, C., Berhanu, T. A., Erbland, J., Savarino, J. & Johnson, M. S. Laboratory study of nitrate photolysis in Antarctic snow. I. Observed quantum yield, domain of photolysis, and secondary chemistry.
- 690 *The Journal of Chemical Physics* **140**, 244305 (2014).
52. Chu, L. & Anastasio, C. Quantum yields of hydroxyl radical and nitrogen dioxide from the photolysis of nitrate on ice. *J. Phys. Chem. A* **107**, 9594–9602 (2003).

- 695 53. Benedict, K. B., McFall, A. S. & Anastasio, C. Quantum yield of nitrite from the photolysis of aqueous nitrate above 300 nm. *Environ. Sci. Technol.* **51**, 4387–4395 (2017).
54. Kaiser, J., Hastings, M. G., Houlton, B. Z., Röckmann, T. & Sigman, D. M. Triple oxygen isotope analysis of nitrate Using the denitrifier method and thermal decomposition of N<sub>2</sub>O. *Analytical Chemistry* **79**, 599–607 (2007).
- 700 55. Morin, S. *et al.* Comprehensive isotopic composition of atmospheric nitrate in the Atlantic Ocean boundary layer from 65 degrees S to 79 degrees N. *Journal of Geophysical Research-Atmospheres* **114**, (2009).
56. Sigman, D. M. *et al.* A bacterial method for the nitrogen isotopic analysis of nitrate in seawater and freshwater. *Anal. Chem.* **73**, 4145–4153 (2001).
- 705 57. Casciotti, K. L., Sigman, D. M., Hastings, M. G., Böhlke, J. K. & Hilkert, A. Measurement of the oxygen isotopic composition of nitrate in seawater and freshwater using the denitrifier method. *Anal. Chem.* **74**, 4905–4912 (2002).
58. Baertschi, P. Absolute <sup>18</sup>O content of standard mean ocean water. *Earth and Planetary Science Letters* **31**, 341–344 (1976).
59. Mariotti, A. Atmospheric nitrogen is a reliable standard for natural <sup>15</sup>N abundance measurements. *Nature* **303**, 685–687 (1983).
- 710 60. Pourchet, M. *et al.* Distribution and fall-out of <sup>137</sup>Cs and other radionuclides over Antarctica. *Journal of Glaciology* **43**, 435–445 (1997).
61. Ding, M. *et al.* Spatial variability of surface mass balance along a traverse route from Zhongshan station to Dome A, Antarctica. *Journal of Glaciology* **57**, 658–666 (2011).
62. Verfaillie, D. *et al.* Snow accumulation variability derived from radar and firn core data along a 600 km transect in Adelie Land, East Antarctic plateau. *The Cryosphere* **6**, 1345–1358 (2012).
- 715 63. Favier, V. *et al.* An updated and quality controlled surface mass balance dataset for Antarctica. *The Cryosphere* **7**, 583–597 (2013).
64. Hoshina, Y., Fujita, K., Iizuka, Y. & Motoyama, H. Inconsistent relationships between major ions and water stable isotopes in Antarctic snow under different accumulation environments. *Polar Science* **10**, 1–10 (2016).
- 720 65. Ding, M. *et al.* Re-assessment of recent (2008 - 2013) surface mass balance over Dome Argus, Antarctica. *POLAR* **35**, (2016).

66. Ekaykin, A. A. *et al.* Underestimation of Snow Accumulation Rate in Central Antarctica (Vostok Station) Derived from Stake Measurements. *Russian Meteorology and Hydrology* **45**, 132–140 (2020).
- 725 67. Sommer, S., Wagenbach, D., Mulvaney, R. & Fischer, H. Glacio-chemical study spanning the past 2 kyr on three ice cores from Dronning Maud Land, Antarctica: 2. Seasonally resolved chemical records. *Journal of Geophysical Research: Atmospheres* **105**, 29423–29433 (2000).
68. Richter, A. *et al.* Surface mass balance models vs. stake observations: a comparison in the Lake Vostok region, central East Antarctica. *Frontiers in Earth Science* **9**, 388 (2021).

730

## Supplementary Files

This is a list of supplementary files associated with this preprint. Click to download.

- [Akersd15NManuscript20220128NComSupplement.docx](#)